Granular Matter manuscript No.
(will be inserted by the editor)

Micromechanics of elastic buckling of a colloidal polymer layer on a soft substrate: experiment and theory

Antoinette Tordesillas · David Carey · Andrew B. Croll · Jingyu Shi · Bekele Gurmessa

Received: date / Accepted: date

Abstract We study the buckling instability of a colloidal particle layer adhered to an elastic substrate using an integrated experimental and theoretical approach. Experiments using monodisperse colloid-scale spherical particles made of polystyrene and silica, show that the wavelength of the initial (critical) buckling mode is independent of particle modulus and linearly dependent on particle radius — in contradiction with the predictions of the prevailing continuum model. We developed a granular model of the particle layer using structural mechanics techniques. The granular model predicts the observed wavelength of the initial, critical buckling mode within the estimated range of parameter values for the experiment. The evolution of this mode into the post-buckling regime is examined. Results highlight the crucial role of material discreteness in the mechanical response, and the need for accurate methods of estimating parameters for the particle-scale resistances against buckling.

Keywords Localisation · Periodicity · Bifurcation · Instability · Buckling

1 Introduction

Buckling instabilities in thin films adhered to thick elastic substrates have recently been the focus of much attention [1–4]. The prevailing theory for the emergence of such sinusoidal buckling patterns in film-substrate composites under compression is derived from a continuum model involving a homogeneous thin elastic film of thickness t on an elastic substrate [1–3, 5]. Under plane-strain conditions, with the film assumed to be much stiffer than the soft thick substrate, the balance between the energy required to bend the film and that required to deform the underlying substrate provides the condition for the onset of buckling. For small strains and small amplitudes of the buckled configuration relative to the wavelength, the critical wavelength λ_C for which the total strain energy is a minimum is [1–3]:

$$\lambda_C = 2\pi t \left(\frac{\bar{E}_f}{3\bar{E}_s} \right)^{1/3}; \tag{1}$$

where $\bar{E}_\alpha = E_\alpha/(1-\nu_\alpha^2)$, E_α is the Young's elastic modulus and ν_α is the Poisson ratio (subscripts $\alpha = f, s$ represent film and substrate, respectively).

The continuum model in (1) has been adapted to study periodic buckling instabilities arising in systems comprising a granular monolayer suspended on a fluid base (e.g. [6]). While the model is able to capture the observed buckling wavelengths, more recent experiments [7, 8] cast light on discreteness as a vital ingredient in modelling the collective behaviour of the particles these systems. In the experiments presented here, we observe buckling instabilities in disaccord with equation (1) and, consequently, propose a granular model to characterise quantitatively the influence of discreteness on mechanical response. Specifically, we take the first steps toward unraveling the micromechanics of buckling instabilities in a granular monolayer on a thick substrate, through an integrated experimental and theoretical approach. From the theoretical side, we perform a structural stability analysis of the *discrete* model. Model predictions are then compared with measurements from a suite of experiments using polystyrene

A. Tordesillas*, D. Carey, J. Shi
Department of Mathematics and Statistics, University of Melbourne, Victoria 3010, Australia
*e-mail: atordesi@unimelb.edu.au

A. B. Croll, B. Gurmessa
Department of Physics, North Dakota State University, Fargo, ND 58108-6050 USA

(PS) and silica (Si) particles which quantify the dependence of the critical wavelength on the elastic modulus and radius of the particles. Our specific objective is to establish whether or not the discrete granular model can reproduce the observed wavelength of the initial critical buckling mode, and the evolution of this mode into the post-buckling regime.

This multidisciplinary effort is underpinned by key advances, particularly from the experimental front in both polymer physics as well as granular media micromechanics. Direct analysis of buckling of so-called "force chains" in two dimensions, in a series of physical experiments [9–11] and numerical simulations [12, 13] for millimeter-scale particles, has shown that buckling instabilities govern the shear strength and failure of dense granular media. Grains in a deforming granular material self-organise to form two classes of structures. The first are the columnar structures of force chains, also known as the strong network [12–15]: these bear the majority of the load and continually align in the direction of greatest compression or major principal stress. The second are cyclic structures comprising mainly the complementary weak network particles which provide lateral support to force chains [16,17]. For two- and three-dimensional systems, these two classes of structural building blocks evolve in a highly cooperative manner, the micromechanical details of their co-evolution govern the different regimes of deformation and the transitions between these regimes [9,16,17]. The direct analysis of the evolution of force chains and their supporting neighbours is currently only possible in physical experiments on 2D photoelastic disk systems, through the techniques developed by Behringer and his group [10,11,15,18]. To date, these constitute the only experimental approach capable of delivering measurements of contact forces as well individual grain positions and kinematics over many stages of the loading history. More recent analysis of photoelastic disk assemblies under cyclic shear from Behringer et al. [11], using a combined structural mechanics, complex networks and dynamical systems techniques, has uncovered details of self-organisation of structural building blocks [9,18]. Favoured cluster conformations reside in distinct stability states, reminiscent of "magic numbers" for molecular clusters. To support axial loads, force chains typically reside in more stable states of the stability landscape, preferring stabilising truss-like, 3-cycle contact topologies with neighboring grains [9,17,18]. The most likely conformational transitions during force chain failure by buckling correspond to rearrangements among, or loss of, contacts which break these 3-cycles [16]. These advancements in the structural micromechanics of buckling and self-organisation in millimeter-scale particles may potentially benefit the optimal design of granular composites. To this end, key knowledge gaps at the fundamental level must first be addressed.

Despite the significant insights into the buckling evolution of force chains, there is still no basic experimental validation of the underlying physics. In particular, no studies have yet been undertaken to explore in both experiment and theory the effect of particle properties (e.g. size, shape, stiffness and surface properties), packing topologies and loading conditions on the resultant buckling mode. This includes sinusoidal or localised buckling modes, as observed from the nanoscale and beyond [4,10]. In this study, we embark on a combined experimental and theoretical program which focusses on the length scales of buckling instabilities for a broader range of granular materials, here beginning with micron-scale particles adhered to an elastic substrate. Of interest are the properties of the critical buckling mode, specifically, how its wavelength depends on particle properties (e.g. size, spring stiffness governing inter-particle interaction), loading conditions and the number of particles in the chain.

In Sec. 2, we present the experimental system. We formulate the granular model of the monolayer on an elastic substrate in Sec. 3. Results from comparing the model predictions against experimental observations are given in Sec. 4. Conclusions are drawn in Sec. 5.

2 The Experiment

The basic experimental set-up consists of a well-ordered monolayer of colloid-scale spherical particles laminated to a soft elastic substrate clamped in a compression stage (Fig. 1(a)). The colloidal layer is imaged with an Olympus Flouview 1000 laser scanning confocal microscope, while the substrate is quasi-statically compressed under plane-strain conditions. A typical sample response in Fig. 1(b,c) shows that the colloidal layer buckles out-of-plane and forms a repetitive undulation. As shown in Fig. 1(d), the confocal observation allows us to determine accurate 3D coordinates for every particle in the system. We focus on two length scales of this buckling pattern: (a) peak-to-peak distance in the compression direction or wavelength λ, (b) peak-to-valley distance in the perpendicular direction or amplitude A.

Elastic substrates were formed with a commercial two part polydimethylsiloxane (PDMS) elastomer (Sylgard 184, Dow Corning). The cured PDMS has fair adhesion to the colloidal particles and its modulus can be easily controlled over several orders of magnitude by mixing various ratios of polymer and prepolymer. After mixing, the PDMS is poured into a form such that many 1 cm $\times$ 8 cm $\times$ 0.5 cm pieces were fabricated in each

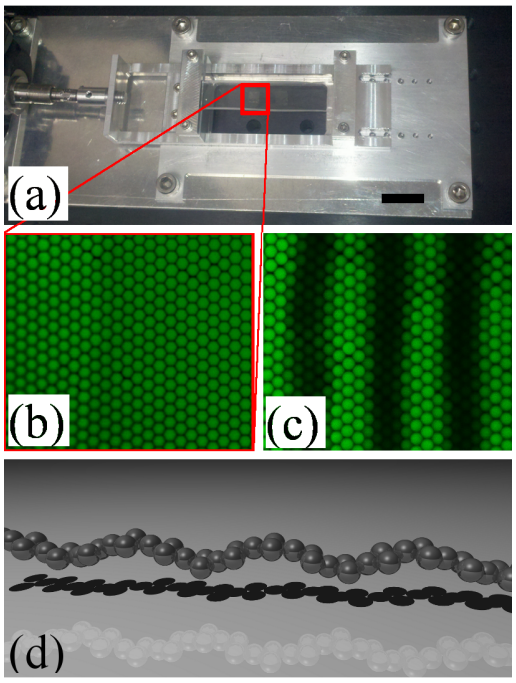

Fig. 1: (a) Photograph of the mechanical strain stage used in these experiments. The stage compression is driven by a motor (Left of image), and a PDMS substrate is shown clamped into the stage. The highlighted region shows a typical sample. A scale bar indicates 20 mm (b) A Laser Scanning Confocal Microscope (LSCM) image of an uncompressed particle monolayer (radius R=1.6 μm polystyrene spheres). (c) The same film under a compressive strain of 10.4%, showing out-of-plane buckling. (d) Data for a typical particle chain rendered in 3D for clarity.

batch. Forms were placed in a vacuum oven, degassed, and annealed at 70°C for 1 hour and subsequently aged an additional 12 hours before use. The adhesive contact details between the particle and film are beyond the scope of this work (and largely understood [19]) but a few comments are warranted. First, there is no experimental evidence that the adhesive contact on the particles changes significantly during a typical experiment (the substrate can to some extent be observed behind the particles). Secondly, because we examine similarly sized silica and polystyrene particles, and find no significant difference in behaviour we can assume that we are not probing adhesion in our experiments. Finally, with large strains and higher modulus PDMS we do observe adhesive failure between the particles and the substrate which we will examine in a later work.

Colloidal monolayers were formed on freshly cleaved mica substrates through a typical drop drying method [20]. Colloidal solutions were created by mixing dry colloids with pure (Milli-Q) water. Colloids shipped in water solution were used as received. Occasionally samples were cooled in order to slow the water evaporation and crystal formation process. After drying, the particle monolayers were transferred to the PDMS substrate by light compression. To aid in the removal of the mica sheet, a drop of milliQ water was placed at the PDMS/mica contact line. Samples were then allowed to dry in air before uniaxial mechanical compression was imposed. Crystal grains were observed if they were within 10° of the direction of applied strain.

Figure 2 shows the typical evolution of the buckling wavelength: the data collapses onto one master curve, a decreasing function of the applied engineering strain $\varepsilon = |\Delta L/L|$, where L is the initial distance between the two strain stage clamps and we neglect an explicit sign as all discussion pertains to compressive strain. The trend appears to be linear in the small to moderate strain region. Importantly, we note that particles of significantly different modulus (polystyrene (PS) and silica (Si)) also collapse onto one master curve. This is a strong indication that the behaviour is independent of the particle properties (e.g. elastic modulus, surface roughness). If the film modulus in (1) is to be associated with the modulus of particles in the granular layer, then this presents a contradiction with continuum theory. Taken together, these provide three observations which can be compared directly with the theory: (a) λ is independent of particle modulus, (b) λ_C is linearly dependent on particle radius R, and (c) $\lambda_C/2R \sim 5.3 \pm 0.4$. Additional results will be shown later in the paper, along with the buckling amplitude A which also collapses onto a master curve that describes a monotonically increasing function of strain.

3 The Model

For the experimental system under plane-strain compression (Fig. 1), we construct a granular model comprising a one-dimensional chain of $N+2$ identical spherical particles, each of radius R, labelled $i = 0, \ldots, N+1$ [21,22]. The chain of particles, adhered to the elastic substrate, is subject to an axial compressive force F (Fig. 3(a)). In two-dimensions, where each particle has three degrees of freedom (two translational, one rotational), the chain of $N+2$ particles has a total of $3N+6$ degrees of freedom. Recall that the particles in the experiment are near-rigid; hence, we can reasonably assume that the distance between adjacent particles is constant (i.e. $2R$) throughout loading. This yields $N+1$ conditions for the $N+1$ contacts, thereby reducing the number of degrees of freedom to $2N+5$. Imposing boundary conditions at the ends of the particle chain further reduce the number of degrees of freedom for each particle i to two: a lateral displacement

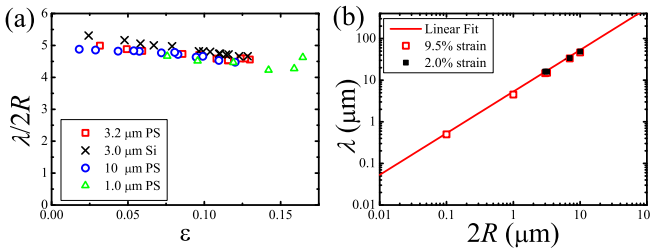

Fig. 2: Typical experimental results. (a) Wavelength λ scaled by particle diameter $2R$, for several different colloidal samples on identical substrates. The average slope extrapolates to a zero strain wavelength of 5.3 ± 0.4. Note the linear relation at small to moderate strain. No difference is seen in the response of polystyrene (PS) and silica (Si) particles, despite a considerable difference between the modulus of silica and polystyrene. (b) Dependence of wavelength on particle radius at two different levels of applied compressive strain.

and rotation, respectively denoted by Rq_i and ω_i, each measured with respect to the initial undeformed configuration (Fig. 3(a)).

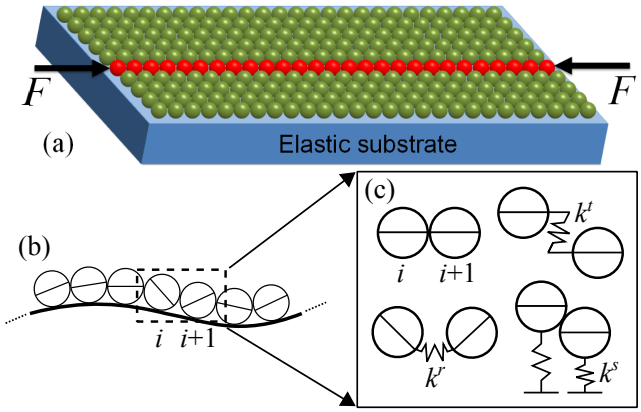

Fig. 3: (a) Initial undeformed configuration of thin monolayer on a very thick substrate (only top part depicted), showing particle chain in layer under axial compression. (b) Buckled configuration of chain showing adjacent particles i and $i+1$. (c) From top left in clockwise direction: particles i and $i+1$ in initial undeformed plane, and spring resistances to relative particle displacement in direction tangential to the contact plane, vertical displacement from undeformed axis of chain, and relative particle rotation, shown with relevant spring stiffness parameters k^t, k^s, and k^r, respectively.

The particles at both ends are free to rotate with the centre of particle $i = 0$ held fixed, while that of particle $i = N + 1$ confined to horizontal translation only, i.e. $q_0 = q_{N+1} = 0$. Buckling (Fig. 3(b)) is resisted by the contact forces and contact moment, each governed by an elastic spring (Fig. 3(c)). The relative tangential force f_i^t is given by $f_i^t = k^t d_i$: k^t is the spring stiffness and d_i is the sliding distance between particles i and $(i + 1)$. Similarly, the contact moment m_i and the lateral support provided by the elastic substrate f_i^s are given, respectively, by $m_i = k^r R^2(\omega_{i+1} - \omega_i)$ and $f_i^s = k^s R q_i$: k^r and k^s are the spring stiffnesses.

The potential energy stored in the buckled particle chain is governed by the work done by the applied axial load F and the interactions between the particles along the chain f_i^t and m_i, as well as between the particle chain particles and the elastic substrate f_i^s. The sliding distance, rolling angle and axial end-shortening between the ith and $(i+1)$th particles is [21,22]:

$$d_i = R\left[2\arcsin\left(\frac{q_{i+1} - q_i}{2}\right) - \omega_{i+1} - \omega_i\right], \tag{2}$$

$$\psi_i = \omega_{i+1} - \omega_i, \tag{3}$$

$$\Delta_i = 2R\left(1 - \sqrt{1 - \left(\frac{q_{i+1} - q_i}{2}\right)^2}\right). \tag{4}$$

Therefore the potential energy function for the complete system can be written as:

$$V = \frac{k^s R^2}{2}\sum_{i=0}^{N+1} q_i^2 + \frac{k^t}{2}\sum_{i=0}^{N} d_i^2 + \frac{k^r R^2}{2}\sum_{i=0}^{N}\psi_i^2 - F\sum_{i=0}^{N}\Delta_i. \tag{5}$$

Summation is taken from 0 to $N + 1$ in the first term to ensure that all end effects are included. No boundary conditions have been taken into account in this equation involving $2(N + 2)$ unknowns, i.e. q_i and ω_i $(0 \le i \le N + 1)$. Due to the nonlinearity of q_i in the expressions for d_i and Δ_i, the potential energy function V given in (5) has nonlinear derivatives with respect to q_i and ω_i. We present below two sets of analysis: (i) the linear analysis of critical buckling in which the small displacement terms in the potential energy function V are linearised, and (ii) the nonlinear analysis of V for the post-buckling regime.

3.1 Linear Analysis of Critical Buckling

The objective of this analysis is to determine the minimum critical buckling load and its corresponding critical buckling mode. When considering the critical buckling point where displacements are small, we may simplify the analysis by linearising the expressions for d_i

and Δ_i, retaining only first-order terms in the series expansions for the arcsine and square root functions. This linearisation results in a so-called 'linearised' potential energy function [21,22]:

$$V_{\rm lin} = \frac{1}{2}k^s R^2 \sum_{i=0}^{N+1} q_i^2 + \frac{1}{2}k^r R^2 \sum_{i=0}^{N} (\omega_{i+1} - \omega_i)^2 + \frac{1}{2}k^t R^2 \sum_{i=0}^{N} (q_{i+1} - q_i - \omega_{i+1} - \omega_i)^2 - \frac{1}{4}FR\sum_{i=0}^{N}(q_{i+1} - q_i)^2 \quad (6)$$

$$\equiv V(q_0, q_1, ..., q_{N+1}, \omega_0, \omega_1, ..., \omega_{N+1}); \quad (7)$$

keeping in mind that linearisation is not performed directly on the potential energy function which, in this case, is in quadratic form.

Consider the buckling of the particle chain under pin-ended boundary conditions: $q_0 = 0, \quad q_{N+1} = 0$. Following [21,23], we expand q_i and ω_i as Fourier modes:

$$q_i = \sum_{m=0}^{N+1} u_m \sin\left(\frac{im\pi}{N+1}\right), \quad (8)$$

$$\omega_i = \sum_{m=0}^{N+1} \phi_m \cos\left(\frac{im\pi}{N+1}\right), \quad (9)$$

with $2(N+2)$ modal amplitudes u_m and ϕ_m $(0 \le m \le N+1)$. The boundary conditions for q_0 and q_{N+1} are automatically satisfied with these modes and thus we can ignore u_0 and u_{N+1} in equation (8). Substituting these modes into the linearised form of V leads to a new potential energy function W of the $2N+2$ modal amplitudes u_m and ϕ_m:

$$W = W(u_1, ..., u_N, \phi_0, \phi_1, ..., \phi_{N+1}). \quad (10)$$

W is in a near-diagonal quadratic form; terms in $u_m u_n$, $\phi_m\phi_n$ and $u_m\phi_n$ are zero for $m \neq n$, whereas those in u_m^2, ϕ_m^2 and $u_m\phi_m$ generally exist. The modal amplitudes u_m $(1 \le m \le N)$ and ϕ_m $(0 \le m \le N+1)$ should be such that the system maintains equilibrium:

$$\partial W/\partial u_m = 0 \quad (1 \le m \le N), \quad (11)$$

$$\partial W/\partial \phi_m = 0 \quad (0 \le m \le N+1). \quad (12)$$

Before proceeding further, note that $\partial W/\partial\phi_0 = 0$ and $\partial W/\partial\phi_{N+1} = 0$ imply $\phi_0 = \phi_{N+1} = 0$. Thus we have $2N$ unknowns: u_m and ϕ_m $(1 \le m \le N)$. The problem can be further simplified by eliminating ϕ_m $(1 \le m \le N)$ from the potential energy function W. To do this, the N first-order equilibrium equations $\partial W/\partial\phi_m = 0$ $(1 \le m \le N)$ are written in the form of a Taylor expansion about the undeflected state:

$$\begin{aligned}\frac{\partial W}{\partial \phi_m} &\approx \left.\frac{\partial W}{\partial \phi_m}\right|_0 + \sum_{j=1}^{N} \frac{\partial}{\partial u_j}\left(\frac{\partial W}{\partial \phi_m}\right)\Big|_0 u_j \\ &\quad + \sum_{j=1}^{N} \frac{\partial}{\partial \phi_j}\left(\frac{\partial W}{\partial \phi_m}\right)\Big|_0 \phi_j \\ &= \left.\frac{\partial^2 W}{\partial u_m \partial \phi_m}\right|_0 u_m + \left.\frac{\partial^2 W}{\partial \phi_m^2}\right|_0 \phi_m \\ &= 0 \quad (1 \le m \le N).\end{aligned}$$

The second equality is due to the fact that W does not contain terms $u_j\phi_m$ and $\phi_j\phi_m$ with $j \neq m$. Thus we have the expression:

$$\phi_m = -\frac{\left(\partial^2 W/\partial u_m \partial \phi_m\right)|_0}{\left(\partial^2 W/\partial \phi_m^2\right)|_0} u_m \quad (1 \le m \le N). \quad (13)$$

As no cross-terms $u_m\phi_m$ appear from the work done by the applied load F, these equations are independent of F. Substituting (13) for ϕ_m in terms of u_m into the W-function, we obtain the diagonalised form of the potential function with N degrees of freedom, which we henceforth write as $A = A(u_1, u_2, ..., u_N)$.

Since the potential function A is in diagonal form, double differentiation of A with respect to each of the u_m in turn leads to a set of N stability coefficients. Letting these stability coefficients be zero, we obtain N critical loads, F_m^C $(1 \le m \le N)$, corresponding to the sinusoidal critical modes or eigenfunctions defined by the integer values of $1 \le m \le N$ in equation (8,9). The minimum critical load, F_{min}^C, and its associated wave number m_{min}, will depend on the relative values of the stiffnesses of the springs that govern the resistances to buckling. As shown in [21], the stability of the initial post-buckling for mode m may be determined from the curvature $\frac{d^2F}{du_m^2}$, evaluated at the critical point C. Finally, accounting for the effects of the normal deformation of particles at contacts introduces extra degrees of freedom into the expressions for the potential energy (5) and (6). This leads to additional equilibrium relations for the extra degrees of freedom which are independent or decoupled from those in (11,12) for the lateral displacements, q_i, $(1 \le m \le N)$ and rotations, ω_i $(0 \le m \le N+1)$. These additional relations will not affect the critical buckling loads and their corresponding buckling modes, since these are solely determined from (11,12). However, the normal deformation of the particles will affect the total length of the buckled particle chain.

3.2 Nonlinear Analysis to Post-Buckling Regime

The full nonlinear potential energy function (5) and the equilibrium conditions require for all $i = 0, \ldots, N+1$:

$$\frac{\partial V}{\partial q_i} = k^s R^2 q_i - \frac{RF}{2}\left[\frac{q_i - q_{i-1}}{\sqrt{1-1/4(q_{i-1}-q_i)^2}} - \frac{q_{i+1}-q_i}{\sqrt{1-1/4(q_i-q_{i+1})^2}}\right] + k^t R^2\left[\frac{2\arcsin\left(\frac{q_i-q_{i-1}}{2}\right) - \omega_{i-1} - \omega_i}{\sqrt{1-1/4(q_{i-1}-q_i)^2}} - \frac{2\arcsin\left(\frac{q_{i+1}-q_i}{2}\right) - \omega_i - \omega_{i+1}}{\sqrt{1-1/4(q_i-q_{i+1})^2}}\right] = 0; \tag{14}$$

$$\frac{\partial V}{\partial \omega_i} = R^2\left[2\omega_i(k^r+k^t) + (k^t-k^r)(\omega_{i-1}+\omega_{i+1}) - 2k^t\left(\arcsin\frac{q_i-q_{i-1}}{2} + \arcsin\frac{q_{i+1}-q_i}{2}\right)\right] = 0. \tag{15}$$

We impose constraints $q_0 = q_{N+1} = 0$, then set the curvature of the chain at each end to zero to reflect a simply supported boundary condition (see [24]). The equilibrium conditions $\frac{\partial V}{\partial q_0} = \frac{\partial V}{\partial q_{N+1}} = 0$ are now satisfied. Similar conditions apply for ω enabling ω_0 and ω_{N+1} to be expressed in terms of the internal degrees of freedom q_1, ω_1, q_N & ω_N. This leaves $2N$ degrees of freedom with $2N$ associated equilibrium conditions. To investigate the post-buckling behaviour, we used the software AUTO [24,25] to find the equilibrium paths under parametric variation, while identifying all possible bifurcations.

4 Results: Model versus Experiment

The granular model was constructed under the assumption of hard (near-rigid) spheres, thus model predictions are independent of the material properties of the spheres, in accordance with the experimental results in Fig. 2(a). To compare the experimental observations against model predictions, we must focus on the influence of particle radius and the three elastic spring resistances to buckling.

4.1 Resistances to Buckling: Estimating Parameters

A method for the accurate estimation of experimental values for the spring stiffnesses representing the strength of the resistances mobilised at the particle scale is currently lacking. Thus a quantitative comparison between experimental observations and model predictions is not possible. Instead, we use a simple scaling argument to estimate the parameters and establish the extent to which the model can qualitatively reproduce observed behaviour. The substrate deformation will resist any displacement, driving the system towards small length scales. The complementary energy which drives the system to larger length scales (bending in the continuum case) does not exist. In this case, it is replaced by the constraints of the contact moment and tangential force acting between adjacent particles in the particle chain. We thus base our estimates of the spring constants from the elastic properties of the substrate. In particular, a reasonable choice for k^s is made by assuming a Hookean constitutive relation for the elastic substrate. Thus $k^s \sim E$ where E is the Young's elastic modulus of the substrate: this yields $k^s = 400$ kN/m. We then consider the critical and post-buckling regimes for two sets of parameters with $k^s = 400$ kN/m. In the first, denoted as P1, we have $\frac{k^r}{k^s} > 1$ and $\frac{k^t}{k^s} > 1$: specifically $k^t = 1100$ kN/m and $k^r = 1000$ kN/m. Parameter set P1 corresponds to the observation that the relative slip and relative rotation between adjacent particles in the experiment were small compared to the vertical displacement. Note that similar relative values for these parameters were used in the force chain analysis of [13] for granular assemblies where resistances at the contacts in the force chain column were stiffer than that of the lateral confining force from the surrounding weak network particles. In the second parameter set, denoted as P2, we set all three spring constants to the same order as E: $k^s = k^t = k^r = 400$ kN/m. In addition, given the uncertainty regarding the range of experimental parameter values, a thorough parametric analysis is undertaken for the critical buckling mode.

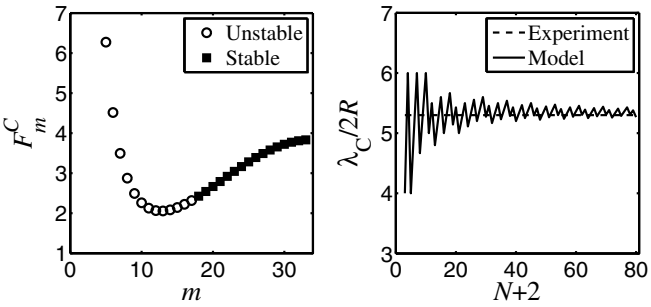

Fig. 4: Model predictions for P1 parameter set and $R = 1.6$ μm. (a) Critical buckling loads for $N+2 = 35$ ($F^C_{min} = 2.06$ N and $m_{min} = 13$). (b) Predicted critical wavelengths consistent with those observed in experiment over a wide range of chain lengths $N+2$, with increasing accuracy as chain length grows.

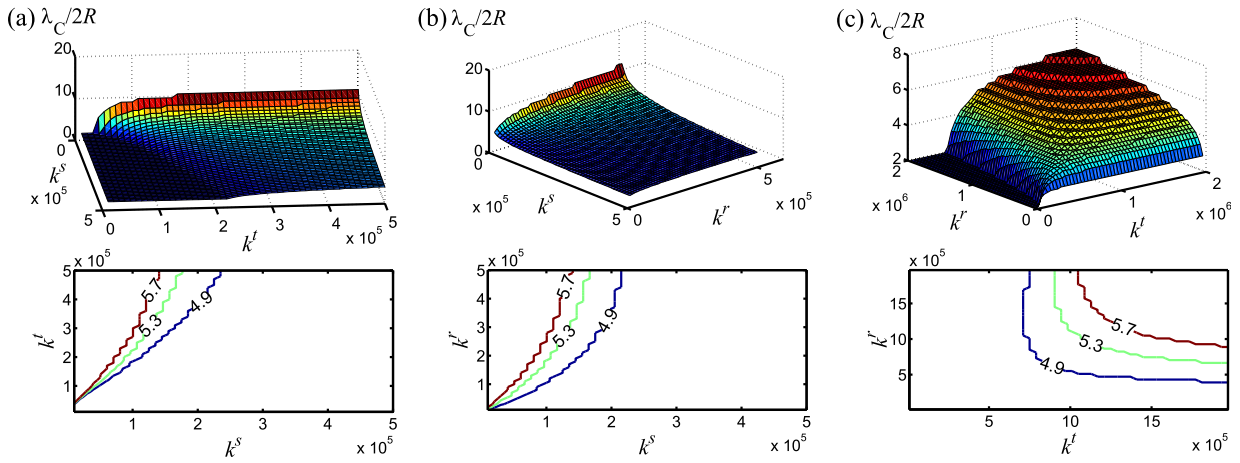

Fig. 5: Predicted influence of stiffness parameters on critical buckling wavelength for $R = 1.0\ \mu$m, $N + 2 = 61$: (a) $k^r = 400$ kN/m, (b) $k^t = 400$ kN/m, (c) $k^s = 400$ kN/m. Contour plots show the range of parameter values which give the experimentally measured critical wavelength $\lambda_C/2R \sim 5.3 \pm 0.4$.

4.2 Critical Buckling Load and Wavelength

Figure 4(a) shows the spectrum of critical buckling loads corresponding to the harmonically varying critical modes or eigenfunctions for parameter set P1. The minimum critical buckling load F^C_{min} occurs at $m_{min} = 13$: this determines a characteristic critical buckling wavelength for this parameter set and chain length [22]. In Fig. 4(b) we see the model predicts an initially oscillatory variation of the critical wavelength with chain length, but the amplitude rapidly decays as chain length grows, giving way to a dominant wavelength that is linearly dependent on the particle radius, in clear agreement with the experiment (Fig. 2(a,b)).

Using parameter set P1, the model predicts critical wavelengths in the range that encompasses the experimental values $\lambda_C/2R \sim 5.3 \pm 0.4$ (Fig. 4(b)). A similar decaying oscillatory trend, as shown in Fig. 4(b), applies for parameter set P2; however the critical wavelength approaches ~ 4 particle diameters. The robustness of λ_C with respect to chain lengths of ~ 30 particles or greater enables us to perform a parametric analysis using a sufficiently long chain, with confidence that any variation in $N + 2$ will not have significant effects on our analysis. In Fig. 5, we consider the effect of varying model spring parameters within the estimated experimental range of parameter values, with a chain length of 61 particles. Observe that increasing the lateral confining stiffness (k^s) drives the critical wavelength down because large displacements become unfavourable. The opposite is seen when the tangential (k^t) and rolling (k^r) stiffnesses are increased; inter-particle sliding and rolling now encounter greater resistance and larger wavelengths emerge. The accompanying contour plots show the multitude of possible parameter combinations which produce critical wavelengths consistent with those observed in experiment.

4.3 Post-Buckling Amplitude and Wavelength

The experimental comparisons in the preceding section pertain to the critical buckling point where the linearised analysis is valid. In order to examine the behaviour in the post-buckling regime, where the assumption of small displacements is no longer valid, the full nonlinear potential (5) must be used. In Figs. 6-8, we employ AUTO to determine the evolution of post-buckling configurations emanating from the initial critical buckling mode $m_{min} = 13$ for a particle chain of 35 particles, using parameter set P1. A particle radius of $R = 1.6\ \mu$m is chosen to enable a direct comparison with a sample set of experimental data points. For P1, m_{min} is unstable (recall Fig. 4(a)). This implies that the granular layer can adopt other configurations in the post-buckling regime, including sinusoidal or localised configurations. While an unstable critical buckling mode is a natural precursor of localisation [22], we see from Fig. 6 that sinusoidal modes are still energetically favoured. This may explain the lack of localisation observed in the experiment. The persistence of sinusoidal buckling configurations into the post-buckling regime is shown in Fig. 7. The predicted increase (decrease) in the amplitude (wavelength) of the buckled configuration with increasing strain is in reasonable agreement with experimental observations: see Fig. 8(a) (Fig. 8(b)). The higher predicted amplitudes in Fig. 8(a) may be due to the substrate in the experiment being an elastic continuum, while that in the

model comprises discrete springs: the continuum substrate will exert an additional resistance to the buckling in the substrate plane that will drive down the amplitude to smaller values. Overall, whilst good agreement between model predictions and the experiments is evident, we note that these findings only suggest that the model has the possibility to reproduce what is observed experimentally. We make no claim that these computed solutions are being exactly replicated in experiment. Like P1, the initial critical buckling mode for P2 proves to be unstable. As earlier mentioned, this is a precursor condition for localised buckling, although the eventual post-buckling configuration (localised versus sinusoidal) ultimately depends on the potential energy pathway. Indeed, in contrast to P1, an analysis of the energy pathways in the post-buckling regime for P2 shows that localised modes are energetically favourable, with buckling localising at one end of the chain. The predisposition to localised buckling in nano- and micro-scale particle systems warrants further investigation, both experimentally and theoretically [4]. In general, many factors govern the post-buckling behaviour including: initial undeformed configuration, particle size distribution, constitutive properties of the particles, and the relative strengths of the various resistances at the grain-grain or grain-substrate/wall contacts. For assemblies of millimetre-size grains, such as those commonly encountered in soil mechanics (i.e. sand) [26], localised buckling is prevalent and believed to be the root-cause of macroscopic failure via shear bands. Indeed, localised buckling modes and their evolution to shear bands were demonstrated in 2D assemblies of photoelastic disks [10,11,15]. We emphasise that, in common with soil mechanics tests, these photoelastic assemblies comprise polydisperse particles and embody force chains which are rarely if ever perfectly straight. By contrast, this study focussed on a monodisperse granular layer with an initially straight configuration. This difference in particle size distribution and initial particle alignment is expected to have a profound influence on buckling behaviour and may thus explain the lack of localisation observed in the present set of experiments.

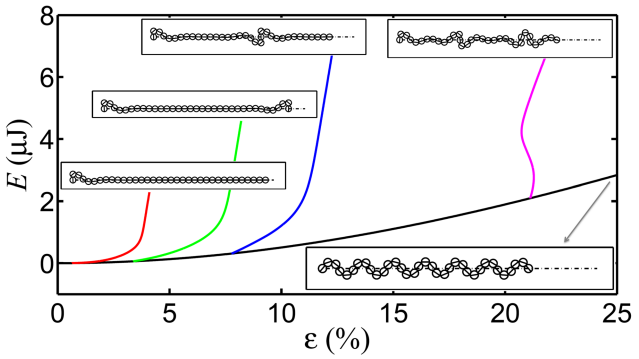

Fig. 6: Energy of post-buckling configurations generated by AUTO for increasing strain emanating from $m_{min} = 13$ with parameter set P1, $R = 1.6$ μm and $N + 2 = 35$. Sinusoidal modes are energetically favoured; bifurcations which lead to localisation are marked by an increase in potential energy.

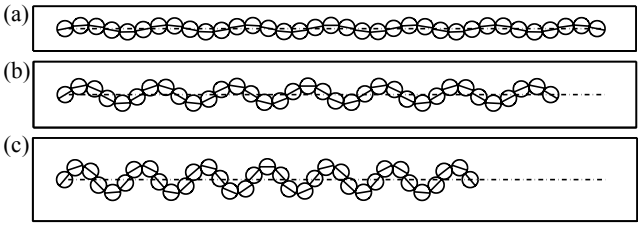

Fig. 7: AUTO generated post-buckling configurations for increasing strain along least energy solution branch emanating from $m_{min} = 13$ with parameter set P1, $R = 1.6$ μm and $N + 2 = 35$: (a) $\varepsilon = 1.35\%$, (b) $\varepsilon = 10\%$, (c) $\varepsilon = 25\%$.

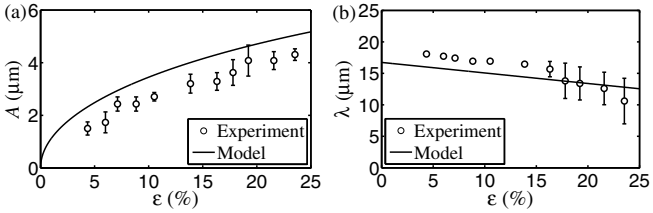

Fig. 8: Comparison between model predictions of (a) amplitude and (b) wavelength (parameter set P1, $R = 1.6$ μm and $N + 2 = 35$) with one representative realisation of experimental measurements: compare with the average measured value in Fig. 2(a) of $\lambda_C = (5.3 \pm 0.4)2R = 16.96 \pm 1.28$ μm.

5 Conclusion and Outlook

We studied the buckling instability of a colloidal particle layer on an elastic substrate using an integrated experimental and theoretical approach. Experiments involving spherical polystyrene and silica particles show that the wavelength of the initial critical buckling mode is independent of particle modulus and linearly dependent on particle radius. A granular model of this system was developed and its structural stability analysed at the critical buckling point, as well as in the post-buckling regime. Simple scaling arguments were used to estimate the possible range of experimental values for the model parameters, i.e. spring stiffnesses of resistances against buckling mobilised at the particle-scale. Experimental observations and model predictions showed

a linear dependence of critical wavelength over a wide range of particle radii. The predicted values varied according to the relative values of the spring stiffnesses, but well encapsulate the measured value (i.e. $\lambda_C/2R \sim 5.3 \pm 0.4$) from experiments. The evolution of the sinusoidal buckling mode into the post-buckling regime was examined. Again, predicted amplitudes and wavelengths were in fair agreement with the experimental measurements.

In closing, we provided experimental evidence of the buckling of a particle chain in a compressed granular layer. Our findings highlight the influential role of discreteness on the mechanical response of the granular layer under constrained compression. It is clear that precise measurement of the grain-scale resistances against buckling is necessary for quantitative prediction. Ongoing work is focussed on this issue coupled with model refinements to account for a wider range of materials from hard to soft particles. Given the surge in interest and technological importance of buckling instabilities, we envision that an improved understanding of the structural micromechanics of buckling in granular composites will find applications in fundamental materials science and many emerging technologies from the nanoscale and beyond. These systems are prone to self-organized pattern formation especially in the lead up to and during failure (e.g. buckling, wrinkling, shear bands etc.). Thus the rational design of granular composites with optimised properties depends crucially on a proper understanding of the transition from the discrete to the continuum and the interaction at the interface – with respect to these patterns of instabilities. To this end, this study casts light on some open challenges and future research directions, both theoretical and experimental. In common with models of other granular-solid interaction systems, realistic computer simulations would greatly complement the structural mechanics approach adopted here (e.g. [27]). The simulations can replicate experiments more faithfully while the structural mechanics approach can deliver more insights into the number and nature of accessible configurational states that the system can potentially inhabit. Realistic simulations may require a coupled Discrete Element Model (DEM) and Finite Element Model (FEM) [27]. In the DEM model of the granular layer, various contact models may be used to represent the interaction at the grain-grain contacts as well as at the grain-substrate contacts: e.g. linear spring-dashpot (Hookean), nonlinear spring-dashpot (Hertz-Mindlin). Coupled with the FEM model of the substrate, one can perform an inverse analysis to establish not just the contact law that is best suited for the system under study, but also generate accurate estimates of the parameters associated with the optimum contact model and constitutive model for the substrate. This theoretical advance needs to be correlated with a series of in-situ measurements, so that rigorous methods can be developed to reliably establish material parameters. Examples of such are optimisation methods in which an error function that quantifies the accuracy of numerical predictions with respect to experimental measurements is minimised. No matter the strategy, a coordinated and highly integrated effort between theory and experiment offers the best way forward.

Acknowledgements We thank our reviewers for their insightful comments and helpful suggestions. A.T., J.S. and D.C. are supported by: US Army Research Office (W911NF-11-1-0175), Australian Research Council (DP120104759) and the Melbourne Energy Institute. A.B.C. is supported by NSF-EPSCoR (EPS-0814442) and ACS PRF (52062-DNI7).

References

1. C.M. Stafford, C. Harrison, K.L. Beers, A. Karim, E.J. Amis, M.R. Vanlandingham, H.C. Kim, W. Volksen, R.D. Miller, E.E. Simonyi, Nature Mater. **3**, 545 (2004)
2. A. Volynskii, S. Bazhenov, O. Lebedeva, N. Bakeev, Journal of materials science **35**(3), 547 (2000)
3. N. Bowden, S. Brittain, A.G. Evans, J.W. Hutchinson, G.M. Whitesides, Nature **393**, 146 (1998)
4. S. Singamaneni, V. Tsukruk, Soft Matter **6**, 5681 (2010)
5. E. Cerda, L. Mahadevan, Phys. Rev. Lett. **90**, 074302 (2003)
6. D. Vella, P. Aussillous, L. Mahadevan, Europhys. Lett. **68**(2), 212218 (2004)
7. B. Leahy, L. Pocivavsek, M. Meron, K. Lam, D. Salas, J. Viccaro, K. Lee, B. Lin, Phys. Rev. Lett. **105**, 058301 (2010)
8. P. Cicuta, D. Vella, Phys. Rev. Lett. **102**, 138302 (2009)
9. A. Tordesillas, Q. Lin, J. Zhang, R. Behringer, J. Shi, J. Mech. Phys. Solids **59**, 265 (2011)
10. A. Tordesillas, J. Zhang, R. Behringer, Geomechanics and Geoengineering **4**, 3 (2009)
11. J. Zhang, T.S. Majmudar, A. Tordesillas, R.P. Behringer, Granular Matter **12**(2), 159 (2010)
12. J.F. Peters, M. Muthuswamy, J. Wibowo, A. Tordesillas, Phys. Rev. E **72**, 041307 (2005)
13. A. Tordesillas, M. Muthuswamy, J. Mech. Phys. Solids **57**(4), 706 (2009)
14. F. Radjai, D. Wolf, M. Jean, J. Moreau, Phys. Rev. Lett. **80**, 61 (1998)
15. T. Majmudar, R. Behringer, Nature **435**, 1079 (2005)
16. A. Tordesillas, D. Walker, Q. Lin, Phys. Rev. E **81**, 011302 (2010)
17. R. Arévalo, I. Zuriguel, D. Maza, Phys. Rev. E **81**, 041302 (2010)
18. A. Tordesillas, D. Walker, G. Froyland, J. Zhang, R. Behringer, Phys. Rev. E **86**, 011306 (2012)
19. V.S. Mangipudi, E. Huang, M. Tirrell, A.V. Pocius, Macromol. Symp. **102**, 131 (1996)
20. N. Denkov, O. Velev, P. Kralchevski, I. Ivanov, H. Yoshimura, K. Nagayama, Langmuir **8**(12), 3183 (1992)
21. G. Hunt, A. Tordesillas, S. Green, J. Shi, Philos. Trans. Royal Soc. **368**, 249 (2010)

22. A. Tordesillas, G. Hunt, J. Shi, Granular Matter **13**, 215 (2011)
23. J.M.T. Thompson, G.W. Hunt, *A General Theory of Elastic Stability* (Wiley, 1973)
24. G. Hunt, J. Hammond, Philos. Mag. **92**, 3483 (2012)
25. E. Doedel, B. Oldeman, *AUTO-07P: Continuation and Bifurcation Software for Ordinary Differential Equations*. Concordia University (2012)
26. M. Oda, H. Kazama, Geotech **48**, 465 (1998)
27. K. Rattanadit, F. Bobaru, K. Promratana, J. Turner, Mechanics of Materials **41**(6), 691 (2009)